Stiffness-driven design and optimization of a 3D-printed composite prosthetic foot: A beam finite Element-Based framework

Article *in* Composite Structures · March 2024

DOI: 10.1016/j.compstruct.2024.118053

CITATIONS
0

READS
38

6 authors, including:

Luca Michele Martulli
Politecnico di Milano
29 PUBLICATIONS **230** CITATIONS
SEE PROFILE

Andrea Sorrentino
Italian National Research Council
205 PUBLICATIONS **5,854** CITATIONS
SEE PROFILE

Marino Lavorgna
Italian National Research Council
260 PUBLICATIONS **6,557** CITATIONS
SEE PROFILE

Composites Structures 2024, 118053

https://doi.org/10.1016/j.compstruct.2024.118053

Stiffness-Driven Design and Optimization of a 3D-printed Composite Prosthetic Foot: A Beam Finite Element-Based Framework

Abdel Rahman N. Althahabi[1], Luca M. Martulli[1*], Andrea Sorrentino[2], Marino Lavorgna[2], Emanuele Gruppioni[3], Andrea Bernasconi[1]

[1]Department of Mechanical Engineering, Politecnico di Milano, Via La Masa 1, I-20156 Milano, Italy

[2]Polymer, Composites and Biomaterials Institute, National Research Council (CNR), Via Previati 1/E, 23900 Lecco (LC), Italy

[3]INAIL, Centro Protesi Inail, Via Rabuina 14, 40054 Vigorso di Budrio (BO), Italy

*Corresponding author: lucamichele.martulli@polimi.it

Abstract

Composite foot prostheses are traditionally produced via lamination, a process that grants high structural efficiency. However, it is an expensive and time-consuming process. Production rate and customizability are thus limited. Additive manufacturing of composites can be a potential solution to these limitations. This work presents a tool to design and optimize Continuous Fiber-Reinforced Additively Manufactured (CFRAM) prosthetic feet using beam Finite Element (FE) modeling. This optimization tool was developed for weight minimization and obtaining a CFRAM prosthesis design matching up to three static stiffness parameters. The design variables were defined through parametrizing the geometry of the prosthesis designed and using the composite structure parameters. Thanks to the versatility of the tool, solutions to multiple optimization and design cases were used to assess different design concepts, such as the shape of the prosthesis (C-shape or J-shape). Also, the tool successfully duplicated the stiffness characteristics of an assumed laminated prosthesis. Finally, the sources of inaccuracy associated with the beam FE modeling approach were identified through a comparison with plane stress FE analysis.

Keywords: 3D-printed Prosthetic Feet; Continuous fiber reinforcement; 3D-printed Composites; Optimal Mechanical Design; Geometry Optimization

1 Introduction

Prosthetic feet are one of the four main components of an inferior limb prosthesis. The other components are a socket, a prosthetic knee, and a pylon [1]. There are various categories of prosthetic feet, such as the most basic one, which is the SACH (Solid Ankle Cushioned Heel), and the articulated prosthetic feet [2].

However, this study focuses on Energy Storage And Return (ESAR) feet. This is because ESAR feet provide better forward propulsion by releasing the energy absorbed throughout stance, during late-stance, thereby increasing comfort and allowing for higher activity levels [2,3]. ESAR prostheses are typically fabricated using laminated carbon fiber-reinforced composites [4]. Although the lamination process allows a higher fiber content and excellent strength-to-weight ratio, it is labor-intensive, time-consuming, and expensive [5,6]. An improvement could be obtained via Additive Manufacturing (AM), as its potential has been recognized for rapid and cost-effective fabrication of prosthetic components [7,8].

AM is a rapid and versatile technology that requires little human intervention and allows significantly larger design complexity without additional costs. This makes it an ideal candidate for mass customization and labor reduction [9–11]. Hence, more opportunities are enabled for designing low-cost foot prostheses [12,13]. This is particularly demanded considering the higher rates of major lower extremity amputation among people with lower economic status [14]. Moreover, especially when using Continuous Fiber-Reinforced (CFR) composites, AM can produce structures with high strength/stiffness to weight ratio [15,16], which are crucial properties in prosthetic applications [17–19].

The potential application of AM to prosthetic feet is already being explored in the scientific literature. South et al. [11] designed a 3D printable ESAR foot to have a similar stiffness behavior to a commercial carbon-fiber prosthesis. Their 3D-printed prosthesis had a significant increase in the structure thickness relative to the commercial one because of applying mono-material AM (no reinforcement). The authors implemented a topology optimization framework to reduce the material volume used. However, the stiffness level of the topologically optimized structure had changed significantly from the one of the initial design [20]. Rochlitz and Pammer [21] designed a 3D printable short fiber-reinforced ESAR foot and tested its structural resistance under vertical loading while it settled on a horizontal platform. The authors demonstrated the need for stronger reinforcement since the yielding of the foot occurred at a low load of about 750 N. Porras et al. [22] conducted static proof tests on a Continuous Fiber-Reinforced Additively Manufactured (CFRAM) prosthesis based on ISO 22675 [23]. According to this standard, these tests are performed by applying a vertical load on the prosthesis while it stands on a platform that is tilted to replicate the heel and forefoot maximum loading conditions in an actual gait cycle [23]. In this case, the prosthesis was capable of bearing a load of more than 4000 N in both heel and forefoot loading conditions with no sign of failures

observed [22]. Their study demonstrated the advantage of utilizing continuous fiber reinforcement, hence, the composite structure considered in this study is a CFR structure. However, it is not enough to design a prosthesis with sufficient strength. For an ESAR foot, stiffness needs to be appropriate as well since it could affect the clinical efficacy of the foot [11].

Experimental investigations and surveys with participating amputees revealed the significant effect of stiffness levels on multiple biomechanical variables such as the roll-over shape and prosthetic ankle push-off work [24]. Also, an appropriate balance needs to be sought in the design process of the stiffness level, since more compliance leads to higher energy return, providing better forward propulsion. On the other hand, a too compliant prosthesis undermines body support [25]. Realizing the impact that stiffness has on ESAR feet performance, the design framework of this study was developed to generate prostheses with appropriate stiffness levels. These were assumed to be those of commercially available ESAR feet.

Researchers already presented some frameworks that serve the same purpose of designing ESAR feet with appropriate stiffness or related parameters. Kathrotiya et al. [26] introduced four design concepts of 3D-printed prosthetic feet and estimated their weight and stiffness at the main stages of the gait cycle using Finite Element (FE) analysis. One concept was selected as the optimal, based on a comparative assessment of the FE analysis results. However, the concepts were only compared to each other and were not assessed based on predefined design criteria. Warder et al. [27] obtained seven different experimental designs of CFRAM prostheses that were iterated upon utilizing information from heel and forefoot loading tests similar to those of ISO 22675 [23]. The stiffness and percent energy return of each design under both loading conditions were assessed based on the energy storage and return criteria of the American Orthotic & Prosthetic Association prosthetic foot project [28]. The implemented design framework demonstrated the potential of reaching a design that satisfies the considered criteria. However, the prescribed stiffness levels were not achieved in both loading conditions simultaneously until the seventh iteration. This indicates the need for a more efficient framework that assists in obtaining appropriate stiffness levels under multiple loading conditions simultaneously, e.g., conditions of the gait cycle stages.

Olesnavage et al. [29] developed a framework to optimize the shape and structure thickness of a 3D printable prosthesis using plane stress finite elements. They developed a cost function called the Lower Leg Trajectory Error (LLTE), which aims to establish the link between the stiffness and geometry of the

prosthesis, and its biomechanical performance [30]. The framework developed is effective at determining the optimal design from among a remarkably wide range of prosthesis designs, resulting in highly customized prostheses. Moreover, further improvements in customization can be achieved by incorporating customizable composite material structures, which are possible to produce using advanced 3D printing technologies. Notably, a new fused deposition modeling process was developed by Markforged, called continuous filament fabrication, which allows for continuous fiber-reinforcement of filaments selectively [31,32]. In addition, the weight of the designed prosthesis is not characterized by LLTE [33]. Hence, the demand for lightweight structures in prosthetic devices [4] could be aided through design frameworks aimed to minimize the weight together with granting proper stiffness behavior.

`In this work, an optimization tool for both the geometry and composite structure of a novel CFRAM ESAR foot was developed. The optimization tool is based on beam FE modeling to improve the efficiency of iterating upon different geometries. A graphical representation of the optimization process was implemented to highlight the trend of reaching a solution throughout the full range of each design variable. The design constraints considered impose similar stiffness behavior of a reference commercial carbon-fiber prosthesis. The design objective was set to minimize the weight of the novel prosthesis. Finally, a plane stress FE model of the design solution obtained was created to verify the stiffness characteristics reached by the optimization tool.

2 Methodologies & Modeling

2.1 Reference Prosthesis Modeling

A Reference Prosthesis (RP) was created using the CAD version of a commercial laminated prosthetic foot, obtained by 3D scanning. The RP consists of the main parts shown in Fig. 1b. The plantar and the upper and lower springs were assumed to be made of laminated Uni-Directional (UD) carbon fiber plies, with stacking sequence $[\,(\pm 45°)_m\,(0°)_n\,]_S$, where the *m* to *n* ratio is constant as shown in Table 1. A thickness of 0.125 mm was considered for each ply [34]. The UD carbon fiber properties considered were also assumed from the literature and are provided in Table 2 [35,36]Table 2.

https://doi.org/10.1016/j.compstruct.2024.118053

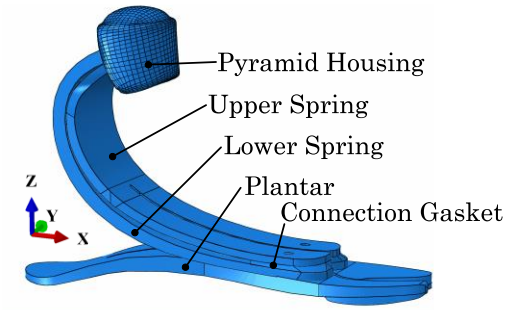

Fig. 1 The RP solid model with the main parts pointed out.

Table 1: The assumed stacking sequence of the laminated plies of each part of the RP.

Part:	Lower/Upper Spring	Plantar
Stacking Sequence:	$[\,(\pm 45°)_2\,(0°)_{16}\,]_S$	$[\,(\pm 45°)_3\,(0°)_{24}\,]_S$

Table 2: The UD carbon fiber laminae engineering constants [35], and density [36]. Moduli are in GPa, Poisson's ratios are dimensionless, and the density is in kg/m^3.

E_{11}	E_{22}	E_{33}	ν_{12}	ν_{13}	ν_{23}	G_{12}	G_{13}	G_{23}	ρ
122.7	10.1	10.1	0.25	0.25	0.45	5.5	5.5	3.7	1460

Considering sagittal plane walking conditions, the deformations are anticipated mainly in the laminae, as a result of bending loads about the y-axis. Therefore, the parts modeled in deformable FEs were the plantar and the upper and lower springs, whereas the pyramid housing was assumed rigid. For simplicity, the connections between the springs and plantar were also assumed rigid.

The RP was modeled using the in-house beam FE modeling MATLAB [37] code used for the development of the optimization tool. To confirm the reliability of this code, the RP beam FE model was assessed against a shell FE model, created on the Abaqus CAE software [38].

2.1.1 3D Shell FE Model

The parts in the shell model, shown in Fig. 2a, were created from the middle surfaces of each original part. Due to the slenderness of the laminae, transverse shear deformations are negligible [39], hence, 4-node

shell elements with 6 degrees of freedom per node were used. The laminated plies of each part, described in Table 1, were embedded in the model utilizing the composite layup tool in Abaqus CAE. The shell parts were rigidly connected at the surfaces highlighted in different colors, as described in Fig. 2a. Also, the pyramid housing was modeled as a rigid coupling between the springs and a node defined on the top of the model (referred to as node-top in the rest of the work). The position of this node was estimated through the solid model as the mid-point of the upper dome-shaped surface of the pyramid housing.

The connection of the prosthesis with the pylon was modeled via specific Boundary Conditions (BC) imposed on node-top. Similarly, the ground contact was modeled through BC imposed on the partition lines representing the heel and forefoot contacts, illustrated in Fig. 2a. The BC simulating the walking conditions studied will be described later in section 2.2.

2.1.2 2D Beam FE Model

The beam model parts, illustrated in Fig. 2b, were created by projecting the shell model on the sagittal plane. This projection leads to the definition of the node-top, node-H, and node-F, which serve the same purpose as node-top and the heel and forefoot contact partition lines of the shell model, respectively (see Fig. 2).

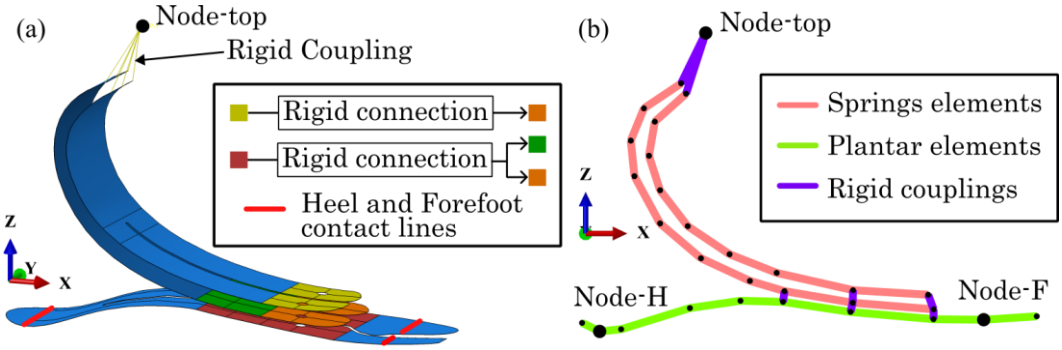

Fig. 2 Models created for the RP: a) shell FE model in Abaqus CAE, and b) beam FE model in MATLAB.

Given that shear flexibility is negligible, as mentioned earlier, 2-node Euler-Bernoulli beam elements with 3 degrees of freedom per node were used. The flexural and axial properties (EI and EA) specified for these elements were determined through homogenization of the composite laminae (Table 1). Therefore, Chou's theory [40] was used to evaluate the elastic modulus along the x-axis of the plies stacked as $[(\pm 45°)_m]$ and

the one of the full laminate, as shown in Table 3. The homogenized modulus of the full laminate is the same for the springs and plantar since the *m* to *n* ratio is constant, as mentioned earlier.

Table 3: Elastic moduli obtained for the RP laminated structure using Chou's theory [40].

Parameter	Description	Value [GPa]
$\bar{E}_{xx}$	Homogenized elastic modulus along the x-axis of the full laminate ($[(\pm45°)_m(0°)_n]_S$ stacking sequence)	102.9
$\bar{E}_{xx}^{(45)}$	Homogenized elastic modulus along the x-axis of the plies stacked as $[(\pm45°)_m]$	19.0

The bending and axial stiffnesses of the beam elements were estimated through Eqn. 1 and 2, respectively:

$$EI = E_{11}I_y^{(0)} + 2\bar{E}_{xx}^{(45)}\left(I_y^{(45)} + A^{(45)}h^2\right) \quad \text{Eqn. 1}$$

$$EA = \bar{E}_{xx}A_L \quad \text{Eqn. 2}$$

where $A^{(45)}$ and A_L are the cross-sectional area of the plies stacked as $[(\pm45°)_m]$ and the ones of the full laminate, respectively. h is the distance between the centroidal axis (parallel to the y-axis) of the plies stacked as $[(\pm45°)_m]$ and the one of the whole laminate. Finally, $I_y^{(45)}$ and $I_y^{(0)}$ are the area moments of inertia of the plies stacked as $[(\pm45°)_m]$ and the ones stacked as $[(0°)_n]$, respectively, each about its centroidal axis. These geometrical parameters were calculated considering a constant width for the prosthesis of 56 mm, which was obtained using the solid model upon neglecting the width variation at specific segments. Accordingly, the flexural and axial properties corresponding to the springs and plantar elements were determined as provided in Table 4.

Table 4: The axial and flexural properties assigned for the beam elements of the RP.

	Springs' elements	Plantar elements
EI [Nmm^2]	4.205×10^7	1.419×10^8
EA [N]	2.880×10^7	4.321×10^7

2.2 Prosthesis Stiffness Parametrization

To show the capabilities of the optimization tool developed, and to evaluate different design approaches, different conditions were analyzed. This led to the definition of six stiffness constraint parameters. The first three parameters characterize the stiffness of a prosthesis at the three critical stages of the stance-phase of the walking gait cycle. These stages are the maximum Heel Loading condition (HL), Mid-Stance (MS), and maximum Forefoot Loading condition (FL) [22]. To simulate these stages, the BC and loads shown in Fig. 3a were imposed, respectively. Node-top was constrained from rotation and translation along the x-axis in the simulations of all stages. A translation constraint along the y-axis was applied to node-H in the simulations of HL and MS, and to node-F in the simulations of MS and FL. Models were, also, oriented by an angle of 15°, 0°, and -20° based on the anticipated ankle-angle in the actual gait cycle at HL, MS, and FL, respectively [23]. By applying a vertical force (F_{az}) and extracting the vertical displacement at node-top, the stiffness (k) at the corresponding stages was computed using Eqn. 3.

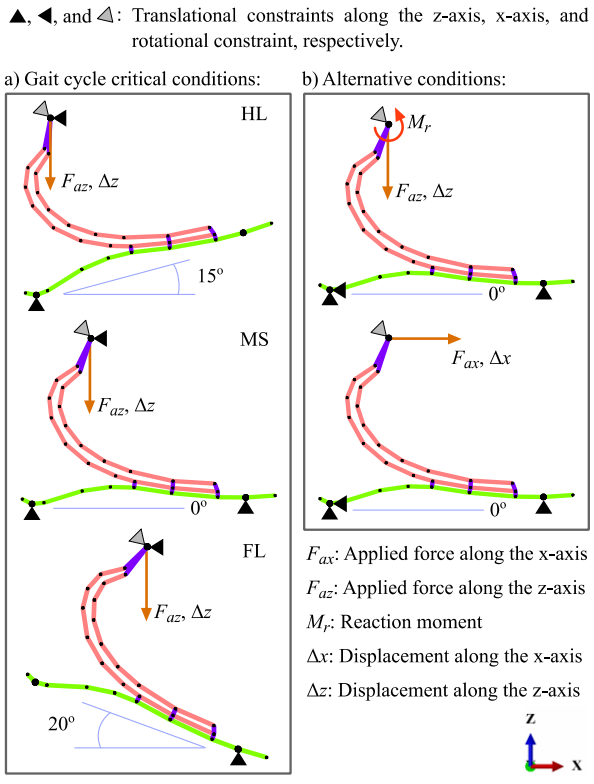

Fig. 3 Boundary conditions, loads, and orientations imposed in beam FE model for the computation of prostheses stiffness at a) the maximum heel loading condition (k_{HL}), Mid-Stance (k_{MS}), and maximum

forefoot loading condition (k_{FL}), in addition to b) the vertical and horizontal stiffnesses (k_z and k_x), and reaction moment factor (Q_m).

$$k_{HL},\ k_{MS},\ k_{FL},\ \text{or}\ k_z = \frac{F_{az}}{\Delta z} \qquad \text{Eqn. 3}$$

The other three parameters were defined, utilizing the concept of the multidimensional mechanics of foot prostheses [41]. These parameters are the vertical (k_z) and the horizontal stiffness values (k_x), and a reaction moment factor (Q_m). Applying the BC and loads illustrated in Fig. 3b, these parameters could be computed using Eqn. 3, 4, and 5, respectively. In these cases, the translational constraint along the x-axis was imposed at node-H instead of node-top, allowing for comparable loading conditions for the estimation of k_z and k_x. Q_m is merely the reaction moment (M_r), defined in Fig. 3b, normalized by the imposed vertical force (F_{az}). This parameter indicates the heel stiffness relative to the forefoot stiffness, i.e., an increased Q_m indicates an increase in the relative heel stiffness. The variation of the heel and forefoot stiffnesses with respect to one another affects the push-off work and energy return during the gait cycle [42]. Therefore, Q_m is useful to consider as one of the stiffness constraint parameters.

$$k_x = \frac{F_{ax}}{\Delta x} \qquad \text{Eqn. 4}$$

$$Q_m = \frac{M_r}{F_{az}} \cdot 100 \qquad \text{Eqn. 5}$$

2.2.1 Design Constraints

In this work, multiple design analyses were performed using the optimization tool developed. The design constraints in these analyses were set based on the values of the six parameters, introduced above, computed for the RP beam FE model. Five beam FE simulations were thus performed as shown in Fig. 3, to estimate the corresponding values provided in Table 5. These values set the benchmark for the design of the novel prosthesis.

Table 5: Stiffness characteristics of the RP obtained through the beam FE model.

k_{HL} [N/mm]	k_{MS} [N/mm]	k_{FL} [N/mm]	k_z [N/mm]	k_x [N/mm]	Q_m [mm%]

168	323	33	323	417	466

2.3 Novel Prosthesis

2.3.1 Prosthesis Geometry

The novel prosthesis will integrate the spring and plantar components into a single 3D-printed part. The possibility of integrating a heel-support as well, similar to designs of other works [21], was investigated. This is to exploit the capability of AM in producing complex geometries. Also, the novel prosthesis was designed to have one spring instead of two, so as to simplify the design process. The point of separation between the spring and plantar geometries was reproduced from the RP model as shown in Fig. 4. However, due to the integration of the spring and plantar into a single part, their center lines in the region of integration are close to one another. This induces a thicker region between the two components to the left of the center lines separation, defined as the spring-plantar junction in Fig. 4. Despite its different thickness, this region was not modeled separately for the sake of simplicity.

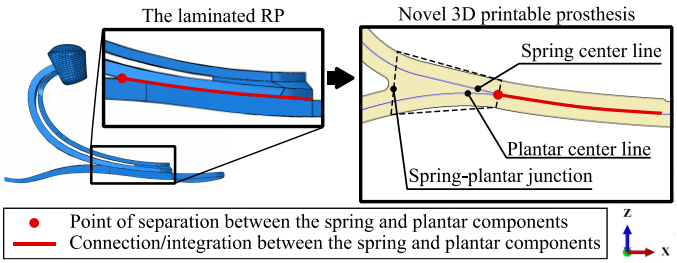

Fig. 4 Illustration of the difference between the RP and the novel prosthesis at the junction between the spring/s and plantar.

The geometry of the novel prosthesis was partially derived from the RP beam FE model such that the plantar geometry and the coordinates of node-top, H, and F were unchanged, as shown in Fig. 5a. Also, the vertical distance between node-top and the spring was adjusted to match the distance between node-top and the lower spring in the RP model. This is to keep the biomechanical performance of the designed prosthesis as close as possible to its reference. Also, this allows the estimation of the parameters defined in section 2.2 for the novel prosthesis applying the same BC described in Fig. 3.

https://doi.org/10.1016/j.compstruct.2024.118053

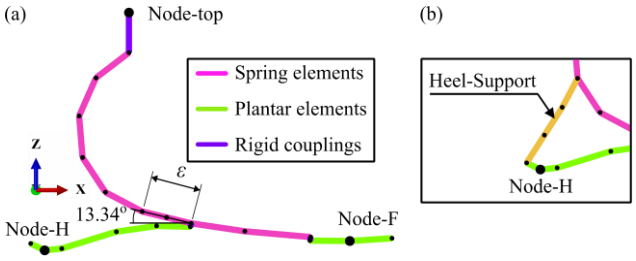

Fig. 5 Illustration of the beam FE modeling of the novel prosthesis, describing a) the spring and plantar, critical nodes, the variable $\boldsymbol{\varepsilon}$, and b) the employment of a heel-support.

On the other hand, the configuration of the spring was designed by the optimization tool developed. Additionally, two common spring shapes were investigated, which are C-shape and J-shape as inspired by the Pro-Flex® XC [43] and Vari-Flex® [44], respectively. These shapes were made customizable by the optimization tool through analyzing a wide range of configurations for each shape. Therefore, a variable, ε, was defined as the length of the spring elements on the left of the spring-plantar separation node as illustrated in Fig. 5a. According to the plantar geometry at this node, these elements were defined oblique at a fixed angle equal to 13.34°. The C-shape was defined by a circular arc that coincides tangentially with the left node of these oblique elements. This circular arc was, also, set coincident to the bottom of the vertical rigid coupling applied to Node-top. The J-shape was defined similarly, however, no verticality constraint was imposed on the rigid coupling. Accordingly, for each of the two shapes, a unique spring configuration could be defined depending on the value of ε. Starting from $\varepsilon = 0$ mm and considering a constant increment, seventy configurations were defined as the geometrical design variable for this study. The sequential variation among the seventy configurations could be demonstrated for both spring shapes, as shown in Fig. 6(see Supplementary Vid. 1). To evaluate the effectiveness of the heel-support presence in enhancing the prosthesis stiffness, each spring shape was investigated with and without a heel-support. In other words, a total of four prosthesis types were investigated.

https://doi.org/10.1016/j.compstruct.2024.118053

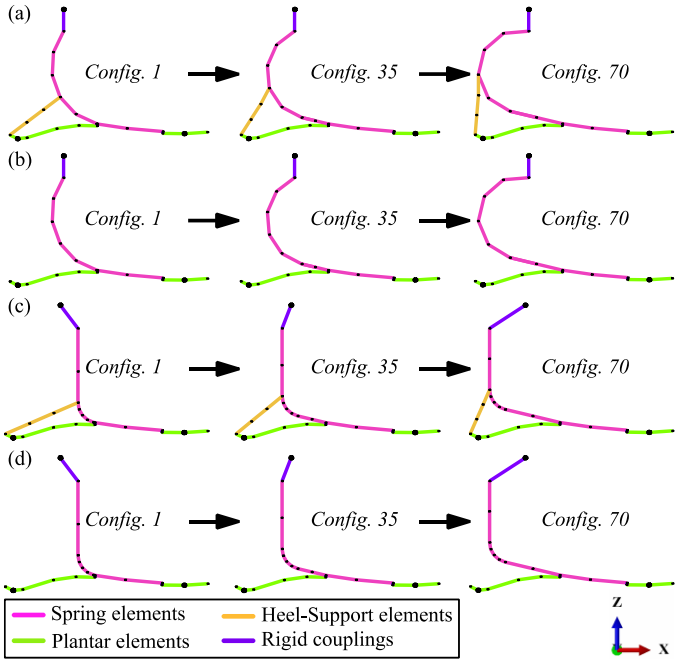

Fig. 6 Illustration of the variation between the spring configurations for thea) C-shaped prosthesis with a heel-support and b) without, and the c) J-shaped prosthesis with a heel-support and d) without.

2.3.2 Prosthesis Material Structure

Continuous filament fabrication allows selecting between CFR and neat/short fiber-reinforced thermoplastic filaments, employing a dual nozzle 3D printing head [32]. This helps limit the usage of continuous fibers in uncritical regions of the structure, leading to a drastic cost reduction, especially when carbon fibers are considered. Therefore, the novel prosthesis was designed to have a lightweight infill core surrounded by a CFR skin. This forms a sandwich composite structure, which is suitable for this application thanks to its structural efficiency. To obtain this structure, the prosthesis needs to be printed on a side. The sandwich structure within the 3D printing set-up is schematically represented as shown in Fig. 7. In this work, the designed sandwich structure was considered composed of continuous carbon fibers for the skin, and 45% triangular Onyx infill for the core. However, the optimization tool developed could be used considering other fibers or infills.

The input parameters adopted for the sandwich composite are reported in Table 6. In this work, the elastic modulus of the skin E_s was assumed equal to that of the tensile modulus of the carbon fiber reinforced filament according to the Markforged datasheet [45]. The width was considered similar to the one assumed

for the RP beam FE model ($b + 2t_{fr}$ = 56 mm). The core and skin thicknesses (c and t_s) are among the design variables of this study.

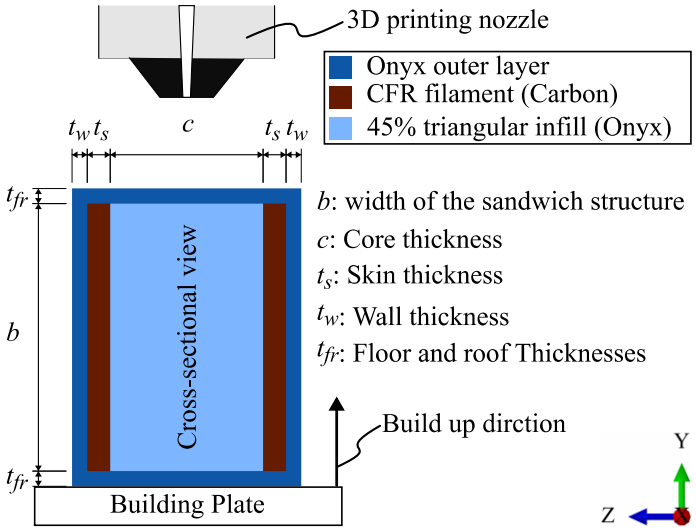

Fig. 7 Schematic of the 3D printing strategy relative to the novel prosthesis material structure.

Table 6: Composite structure details adopted in the optimization procedure.

Parameter	Description	Value
E_s	Modulus of elasticity of the skin [MPa]	60000 [45]
G_c	Shear modulus of the core [MPa]	109 [46]
t_{fr}	Thickness of the floor & roof [mm]	0.5 [47]
t_w	Thickness of the walls [mm]	0.8 [47]
ρ_c	Density of the core [kg/m^3]	477 [46]
ρ_o	Density of Onyx [kg/m^3]	1200 [45]
ρ_s	Density of the skin [kg/m^3]	1400 [45]
b	Width of the composite sandwich [mm]	55

Due to E_s being significantly lower than the elastic modulus of laminated carbon fiber (Table 2), the slenderness ratio of the novel prosthesis structure is anticipated to be significantly lower. This motivated

using Timoshenko beam elements for the modeling of the novel prosthesis to account for shear flexibility. The flexural and axial properties of these elements were estimated through Eqn. 6 and 7, respectively. In these equations, it is assumed that bending and axial loads are only borne by the skins. This is because the tensile modulus of the skin is significantly higher than the one of the core. According to [48], the shear stiffness could be estimated through Eqn. 8. Note that the Onyx outer layer is negligible due to its relatively low thickness and elastic modulus. Nevertheless, it was taken into account for the estimation of the weight of the prosthesis, as will be described in section 2.4.1.

$$EI = E_s\left(\frac{bt_s^3}{6} + \frac{bt_s(c+t_s)^2}{2}\right) \quad \text{Eqn. 6}$$

$$EA = 2E_s bt_s \quad \text{Eqn. 7}$$

$$GA = \frac{b(c+t_s)^2}{c} G_c \quad \text{Eqn. 8}$$

The spring and plantar beam elements were differentiated in Fig. 5a since they were assigned independent properties. These properties are similar in terms of the skin thickness (t_s), since continuous filament fabrication imposes the same number of CFR layers around the whole structure [47]. However, they can be different in terms of the core thickness (c), thus, another design variable, q, was defined as shown in Eqn. 9.

$$q = \frac{c_p}{c_s} \quad \text{Eqn. 9}$$

Where c_s is the core thickness assigned specifically to the spring elements, and c_p is the one of the plantar. Given that the spring is subject to more bending load, it was considered to be thicker than the plantar, as it was designed in similar works [11]. This was imposed by considering c_s as an independent design variable and limiting q from having a value higher than one. In the case of applying a heel-support, as shown in Fig. 5b, the ratio of its core thickness to the one of the spring was assumed as a constant equal to 0.5.

2.3.3 Solution Assessment Models

To assess the design solution obtained in the form of a beam FE model using the optimization tool developed, planar modeling was considered an accurate approach. This is because planar modeling can

https://doi.org/10.1016/j.compstruct.2024.118053

better describe a design made by an in-plane 3D printing approach like continuous filament fabrication. Particularly, plane stress finite elements were utilized similarly to other works [29]. To this aim, two plane stress models were created, as shown in Fig. 8. The printable model replicates the prosthesis structure as it is supposed to be 3D-printed. It was created as a single part with the CFR filament only included at the edges of the core. On the other hand, the interpretive model was created as an assembly of the heel and the spring. This is to establish a plane stress model that is similar to the beam model in terms of the heel length and the CFR filament distribution.

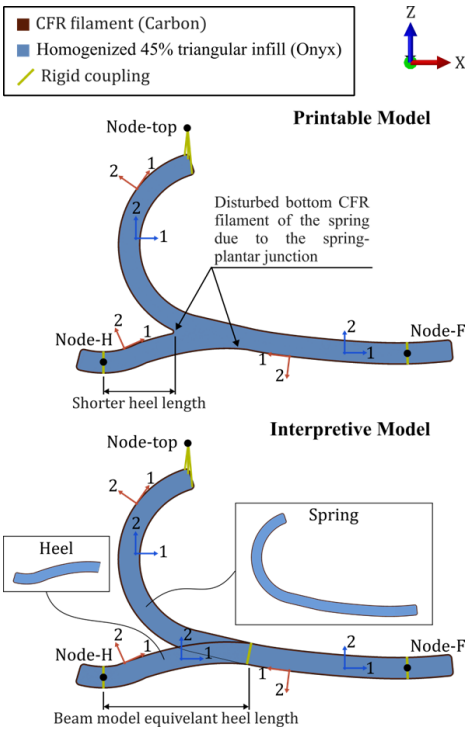

Fig. 8 The plane stress FE models created for the assessment of the prosthesis design found in beam finite elements using the optimization tool developed. Axes 1–2 indicate material orientation.

Similar to the beam model, the plane stress models only included the CFR skin and the infill core, while the Onyx outer layer was neglected. For simplicity, a homogenized infill core was considered. The properties of the CFR filament and the homogenized core infill used in the plane stress models were those reported in Table 7**Error! Reference source not found.**. The corresponding material orientations were assigned based on the continuous fibers direction for the skin and the global coordinate system for the homogenized infill, as described in Fig. 8**Error! Reference source not found.**.

Table 7: Engineering constants used in the plane stress FE models shown in Fig. 8**Error! Reference source not found.**.

Material	E_1 [MPa]	E_2 [MPa]	ν_{12}	G_{12} [MPa]
CFR filament (Carbon)	60000 [45]	2400[1]	0.28[1]	267[1]
Homogenized 45% triangular infill (Onyx) [46]	400	419	0.318	109

[1] Constants determined through the rule of mixture, assuming the Carbon fiber and Nylon properties in [49] and [46], respectively.

2.4 Optimization and Design Cases

The optimization tool was developed to determine the values of three design variables, two of which are parameters of the sandwich structure, and they are interchangeable. In this work, three of the sandwich structure parameters were used interchangeably, which are c_s, t_s, and q. The third design variable is the different configurations (*Config. 1* to *70*) defined by the value of ε, as mentioned earlier. The design constraints are, also, assigned interchangeably considering the determined stiffness characteristics of the RP, presented in Table 5.

An optimization case was set considering one design constraint as shown in Fig. 9a. In addition, two design cases were set considering three constraints per case as shown in Fig. 9b, utilizing the characteristics presented in Table 5 entirely. The optimization case was solved for the four prosthesis types, defined earlier in section 2.3.1, to obtain preliminary prosthesis designs. Then, the design cases were used to potentially refine the prosthesis designs. In case exact solutions exist for both design cases, case I solution has priority since its design constraints simulate the gait cycle conditions, as mentioned earlier in section 2.2. Eventually, one final prosthesis design was preferred and considered for the solution assessment, presented later in section 3.4.

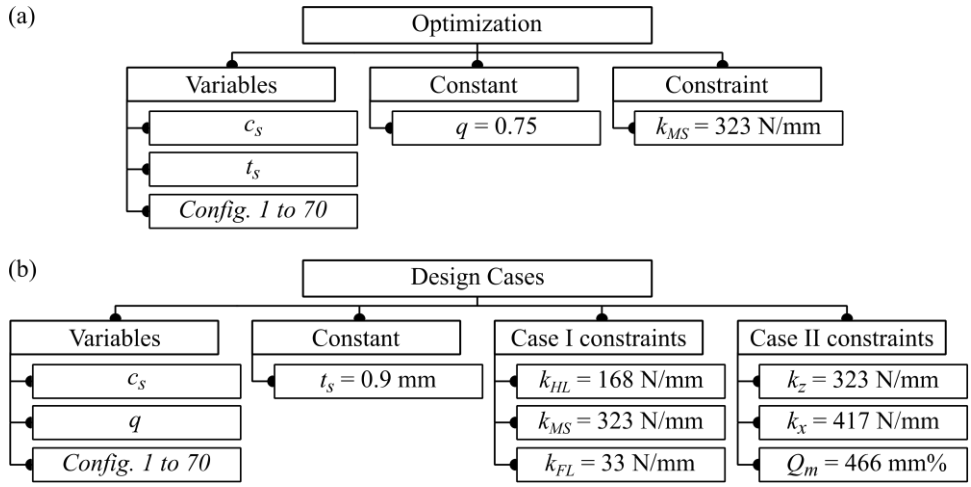

Fig. 9 Description of the parameters considered as design variables or given a constant value, and the applied design constraints in the a) optimization performed, and b) the design cases solved.

In the optimization case, q was assumed as a constant equal to 0.75, and t_s was applied as a variable. However, when 3D printability is considered, t_s is constrained to be an integer multiple of 0.9 mm, which is the carbon fiber reinforced filament thickness according to Markforged [50]. Therefore, q was substituted for t_s in the design cases, so as to allow finding a feasible solution considering the equal number of design variables and constraints.

The optimization and design cases (Fig. 9) were solved by applying a single framework as will be described in section 2.4.1.

2.4.1 Optimization Tool

The optimization tool was developed using MATLAB, utilizing the in-house beam FE modeling code, as mentioned earlier. Its objective function, to be minimized, was set as the weight of the prosthesis, which was estimated using Eqn. 10.

$$Weight = c_s\left(L_s + qL_p + 0.5L_h\right)\left(b\rho_c + 2t_{fr}\rho_o\right) + 2\left(t_s\rho_s b + 2t_{fr}(t_s + t_w)\rho_o + t_w\rho_o b\right)\left(L_s + L_p + L_h\right) \quad \text{Eqn. 10}$$

In Eqn. 10, L_s, L_p, and L_h are the total length of the beam elements representing the spring, plantar, and heel-support, respectively. In the absence of the heel-support, L_h is equal to 0 mm. The optimization is performed through two phases as represented in Fig. 10. In the first phase, the optimization of the sandwich

structure variables is performed. The values of these variables that satisfy the design constraints are found by the tool. When more than one solution is found per configuration, the optimal one is recorded. This is performed and demonstrated through a 2D design chart for each configuration until all configurations are analyzed for. In the second phase, if a solution existed for more than one configuration, the optimal of these solutions is considered as a design output. One of the features of this tool is displaying a moving 2D design chart corresponding to the configuration series, which assists in seeking an approximate solution in case no solution exists.

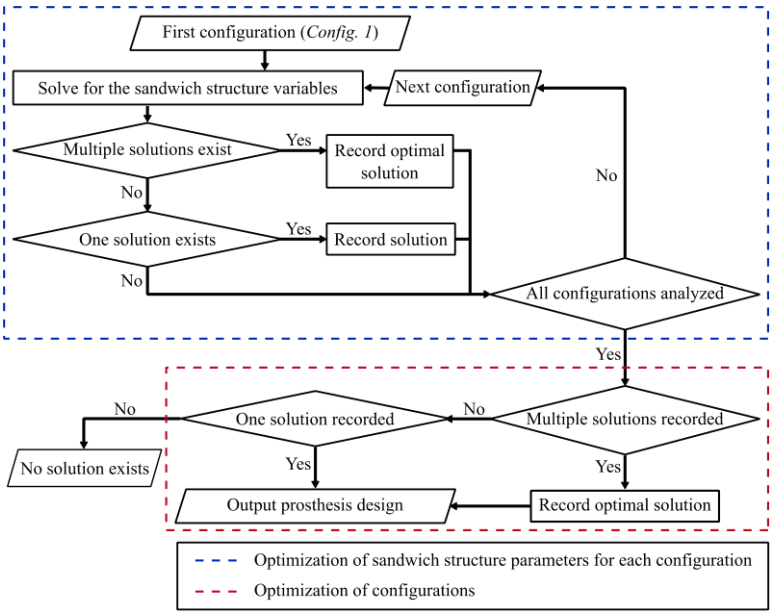

Fig. 10 Flowchart of the design framework applied in the optimization tool developed through MATLAB. The first and the second phases of optimization are distinguished by the blue and red dashed rectangles, respectively.

3 Results & Discussion

3.1 Beam FE Modeling Validation

The values of k_{HL}, k_{MS}, and k_{FL} of the RP were estimated using the beam and the shell FE models shown in Fig. 2. A comparison between both models in terms of these parameters was made to validate the beam FE modeling approach introduced in section 2.1.2. As shown in Fig. 11, the models predict similar values with a maximum difference of 8% for k_{MS}, hence, the modeling approach is validated. For all of the parameters compared, the beam model predicts a stiffer behavior. This is because the width variation of the

RP was neglected in the beam model, as mentioned earlier in section 2.1.2, while the shell model accounts for its exact width.

This shows the capability of beam FE modeling in predicting the stiffness accurately even for structures with high geometrical complexity such as the RP. However, the RP is made from an assembly of composite laminates, which is a different scenario from the novel prosthesis that is 3D-printed as a single sandwich structured part. Considering the latter case, the plane stress FE models (Fig. 8) were dedicated to a detailed assessment of the solutions obtained, as will be discussed in section 3.4.

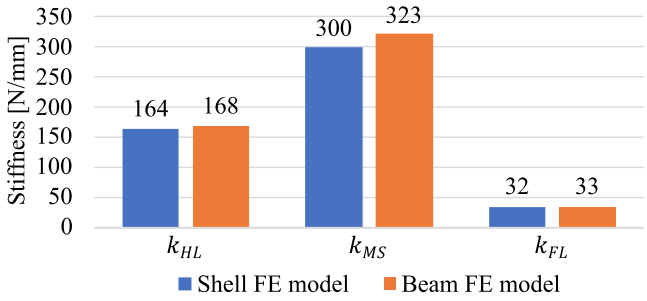

Fig. 11 Comparison of the RP stiffness characteristics estimated through the shell and the beam FE models.

3.2 Preliminary Optimization

The optimization case defined in Fig. 9a was solved for the four prosthesis types, defined in section 2.3.1, through the optimization tool developed (Fig. 10). By applying one design constraint only, it was possible to obtain the optimal sandwich structure parameters for each configuration. The weight of the optimal solution of each configuration of the four prosthesis types is presented in Fig. 12, which shows the optimal configuration for each solution. The optimal sandwich structure parameters at the optimal configurations are shown in Fig. 13. Considering the C-shaped prosthesis, the optimal configuration was found to be *Config. 18*. While this solution demonstrated the ability to reach the optimal configuration, the rest of the solutions were obtained at the boundaries of the range of configurations considered (*Config. 1* or *70*). This indicates the potential existence of the optimal solution beyond this range. A more comprehensive demonstration of the optimal solution realization is shown in Supplementary Vid. 2, and the summary of the solutions obtained is shown in Fig. 14.

.

https://doi.org/10.1016/j.compstruct.2024.118053

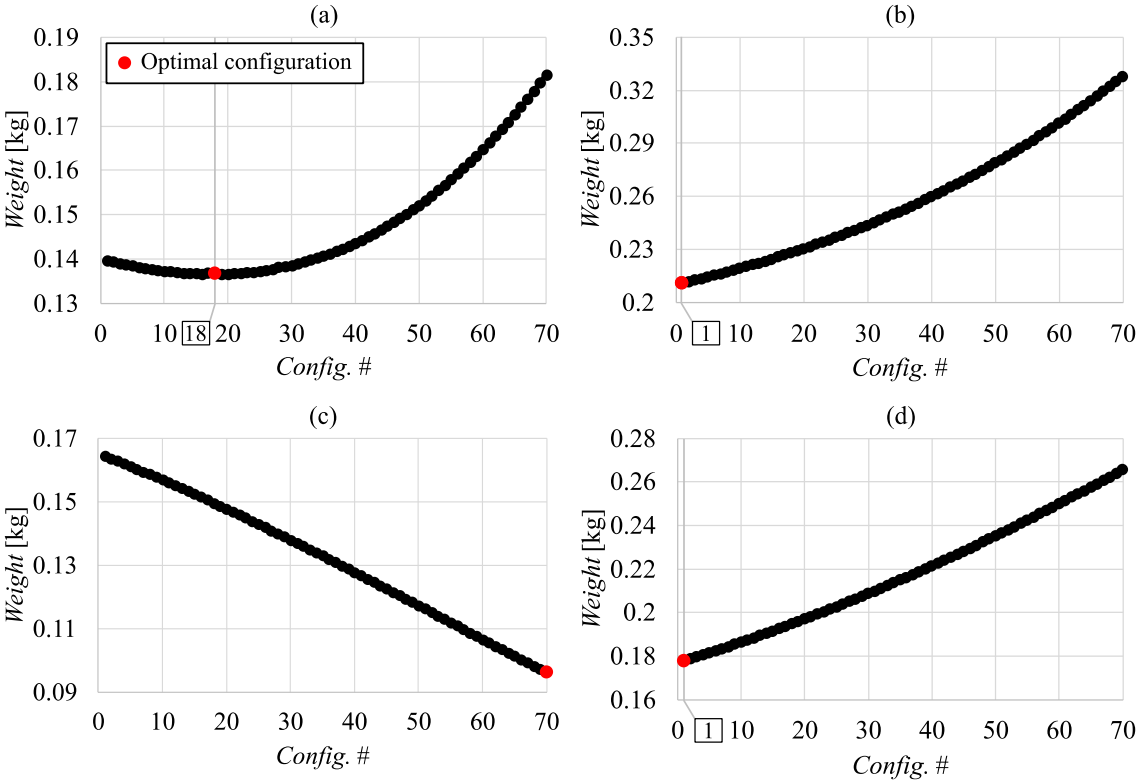

Fig. 12 Weight of the optimal sandwich structure design obtained for each configuration of the four prosthesis types: (a) the C-shaped prosthesis with a heel-support, (b) the C-shaped prosthesis, (c) the J-shaped prosthesis with a heel-support, and (d) the J-shaped prosthesis as a solution of the optimization case defined in Fig. 9a.

https://doi.org/10.1016/j.compstruct.2024.118053

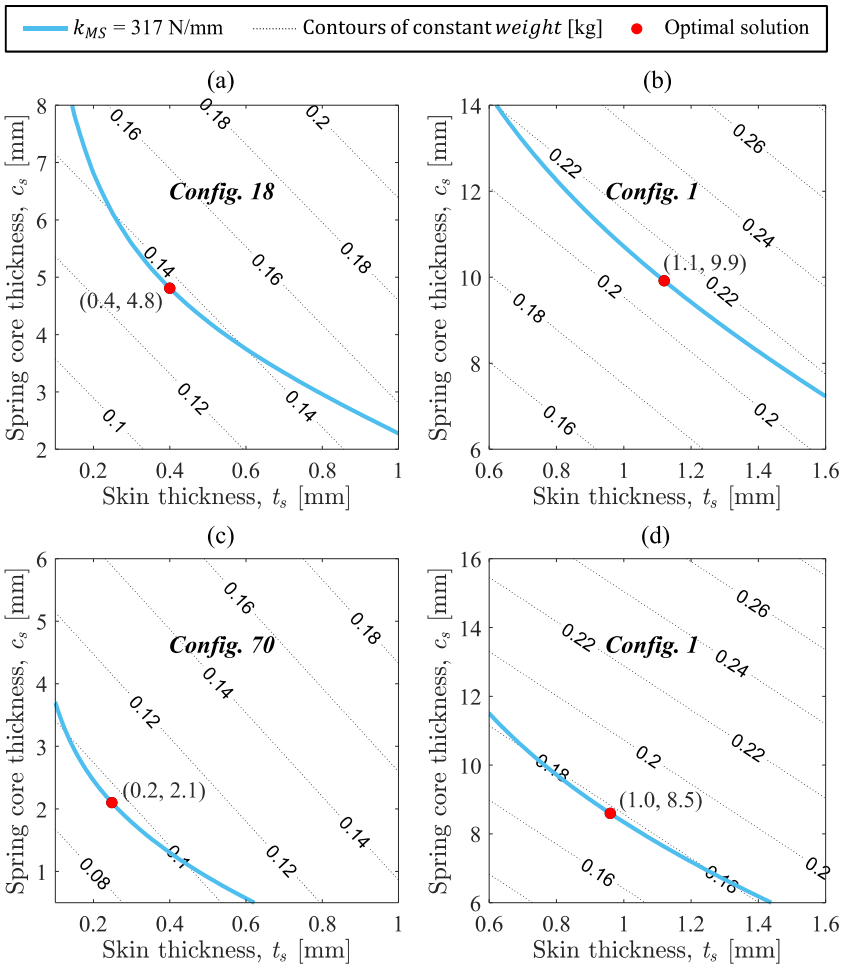

Fig. 13 Solution of the optimization case defined in Fig. 9a in terms of the sandwich parameters at the optimal configuration, solved for the four prosthesis types: (a) the C-shaped prosthesis with a heel-support, (b) the C-shaped prosthesis, (c) the J-shaped prosthesis with a heel-support, and (d) the J-shaped prosthesis.

The solutions indicate that the heel-support had a significant effect on the optimal spring configuration. Its presence allowed the spring to be configured more towards the heel, while its absence restricted the configuration to be closer to the forefoot. Moreover, the heel-support contributed significantly to k_{MS}, resulting in too small t_s values that are not possible to print. This is given the carbon fiber reinforced filament thickness [50], which restricts t_s to be an integer multiple of 0.9 mm, as mentioned earlier. Therefore, the prostheses without a heel-support were preferred for the continuation of the design process.

Moreover, the solutions indicate that the J-shaped spring is stiffer than the C-shaped, which is expected. This is because the C-shaped spring exhibits higher bending deformations when loaded vertically. Since both shapes led to similar results, both were considered in the solution of the design cases, as will be discussed in the next section.

https://doi.org/10.1016/j.compstruct.2024.118053

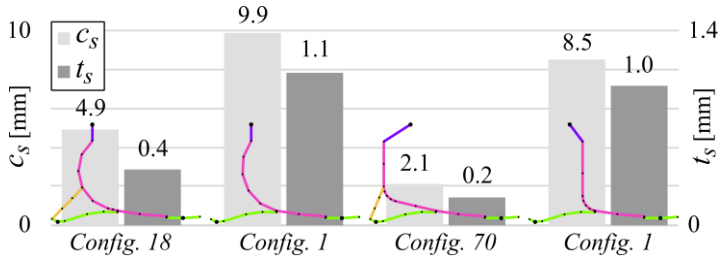

Fig. 14 Summary of the preliminary designs obtained through solving the optimization case defined in Fig. 9a for the four prosthesis types defined in section 2.3.1.

3.3 Design Solution

The design of the C-shaped and J-shaped prostheses without a heel-support was refined by solving the design cases defined in Fig. 9b. No solution was found for Design Case I. On the other hand, solutions were obtained for Design Case II at *Config. 43* and *Config. 58* of the C-shaped and J-shaped prostheses, respectively, as shown in Fig. 15. A demonstration of the results of both design cases obtained for the C-shaped prosthesis is provided in Supplementary Vid. 3. The results indicate that although the designs obtained preserve some stiffness characteristics from the RP, they don't have similar stiffness characteristics in all of the stance-phase critical stages. As shown in Fig. 16, similar k_{MS} values were achieved, however, the k_{HL} and k_{FL} are significantly higher. Therefore, the designs obtained are not expected to have comparable biomechanical performance to the RP. However, the solutions demonstrated the capability of the optimization tool to generate prosthesis designs that satisfy three required stiffness characteristics.

The solution of the J-shaped spring has a weight of 0.25 kg, which is lower than that of the C-shaped solution (0.27 kg). This is because the J-shaped spring is stiffer than the C-shaped, as mentioned earlier. Both of these weights are lower than that of the RP laminae, which was found using the shell CAD model to be equal to 0.35 kg. This indicates the potential of designing CFRAM prosthetic feet with comparable or lower weight than the laminated composite ones.

https://doi.org/10.1016/j.compstruct.2024.118053

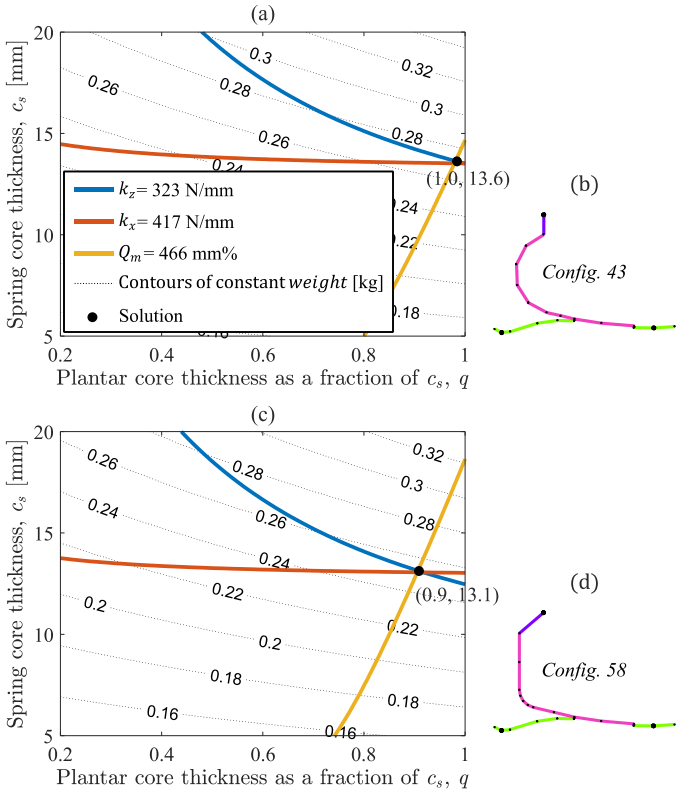

Fig. 15 Solutions of design case II, defined in Fig. 9b, where the design chart (a) corresponds to b) *Config. 43* of the C-shaped prosthesis, and the design chart (c) corresponds to d) *Config. 58* of the J-shaped prosthesis at which the solutions were found.

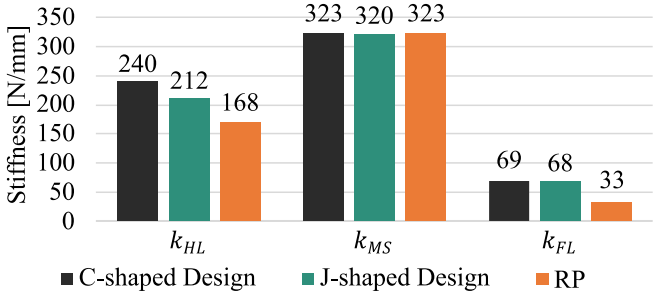

Fig. 16 Assessment of the design solutions of the C-shaped and J-shaped prostheses with respect to the RP in terms of the stiffnesses at the critical stance-phase stages ($\boldsymbol{k_{HL}}$, $\boldsymbol{k_{MS}}$, and $\boldsymbol{k_{FL}}$).

3.4 Solution Assessment

A solution assessment was performed for the C-shaped prosthesis design obtained in section3.3 using the plane stress models described in section 2.3.3. The values of k_{HL}, k_{MS}, and k_{FL} found through the beam model were compared to those estimated through the plane stress models, as shown in Fig. 17. The printable model estimates higher k_{HL} and k_{MS} compared to the beam model, mainly because it has a shorter heel due

to the spring-plantar junction. Oppositely, it estimates a lower k_{FL}, because it lacks the bottom CFR filament of the spring at the spring-plantar junction. This led to a significant stiffness reduction since the forefoot loading is mainly borne by the spring. However, the interpretive model resulted in comparable estimations to those of the beam model. This is because it replicates the simplification considered in the beam model related to the negligence of the spring-plantar junction, as mentioned in section 2.3.1. This explains that the main cause of the discrepancy between the beam model and the printable model is this simplification.

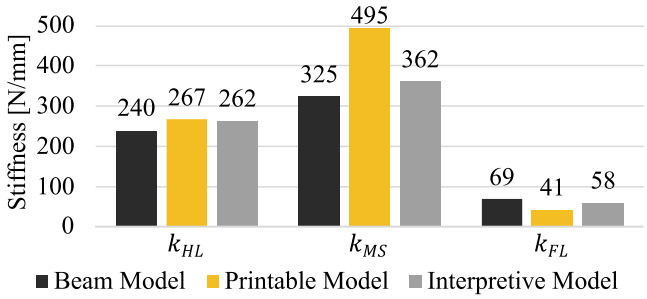

Fig. 17 Assessment of the designed prosthesis beam FE model with respect to the plane stress FE models shown in Fig. 8**Error! Reference source not found.** in terms of the stiffnesses at the critical stance-phase stages ($\boldsymbol{k_{HL}}$, $\boldsymbol{k_{MS}}$, and $\boldsymbol{k_{FL}}$).

From another perspective, the interpretive model predicts a stiffer behavior in the heel loading and mid-stance conditions, whereas a lower stiffness behavior in the forefoot loading. This is because the C-shaped spring leads to compressive stresses in the infill core when loaded in bending, which are not accounted for in beam FE modeling. To elaborate on this, a comparison was made between the stiffness behavior of both models, considering the loading conditions described in Fig. 18a. A vertical force was applied at node-F, while one of the nodes or node sections, highlighted in blue, was fixed. The models were compared by computing the percent difference between the vertical displacement at node-F estimated by each model, as shown in Fig. 18b. The percent difference is nearly constant when the fixed node/node section is 1, 2, or 3. However, the difference exhibits a drastic variation when the fixed constraint is applied beyond these nodes/node sections. This indicates that the beam model estimates the displacement consistently with the plane stress model, when the loaded sandwich structure is nearly straight (between node-F and 3). However, this consistency is disturbed when the curved part of the structure is involved (C-shape). This represents a limitation to the beam FE models of sandwich structures in foot prosthetic applications.

https://doi.org/10.1016/j.compstruct.2024.118053

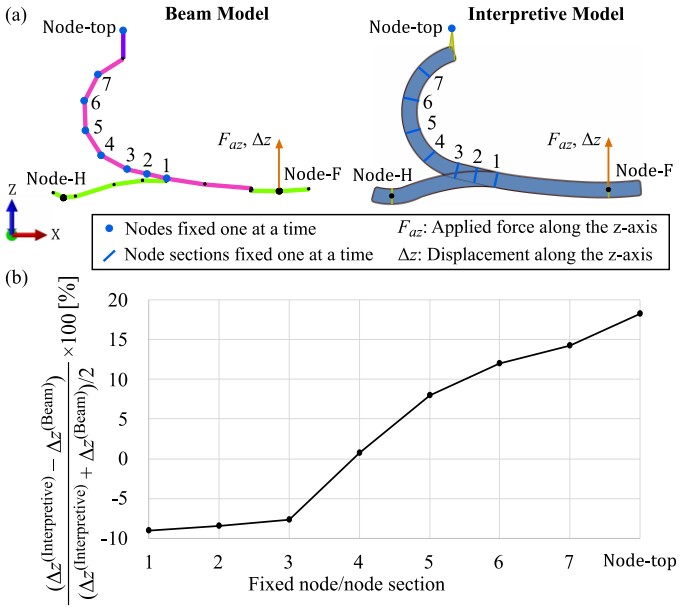

Fig. 18 The effect of the C-shape on the difference between the beam and the plane stress FE models in terms of stiffness prediction. a) Description of the loading conditions applied for making the comparison, and b) the percent difference of the estimated **Δz** at node-F given one fixed node/node section at a time.

3.5 Potentials and Future Developments

The solution assessment, discussed in section 3.4, revealed a couple of limitations associated with the validity of the solution obtained using the optimization tool developed. However, to the best of our knowledge, this study made the first attempt toward a numerical optimization tool for CFRAM ESAR feet. In addition, it sheds light on some of the possible difficulties. Despite having similar efforts, in the literature, for optimizing prosthetic feet [29,51], none of these works aimed to optimize CFRAM ESAR feet.

The current work suggested a versatile and quick optimization tool for CFRAM ESAR feet. The tool is advantageous for obtaining preliminary designs, and enables a fast comparison of a wide range of design possibilities. For example, the preliminary optimizations performed could be repeated for different design variables and constraints to obtain new results related to 280 prosthesis configurations within approximately 5 minutes. Moreover, a new design solution could be obtained considering another set of stiffness constraints, which could be defined by various BC and prosthesis orientations, within an average time of approximately 4 minutes.

Therefore, the utilization of the optimization tool developed can precede the adoption of detailed and more computationally expensive methodologies that resemble the ones of other works [29]. This reduces the time

required during the initial design phase of a CFRAM ESAR foot, facilitating a more streamlined development process for such a new field.

Future works could include the development of an approach to estimate the spring-plantar junction size based on the sandwich structure thickness, which would be embedded in the optimization framework. This will allow modeling the heel with a better approximation of its actual length, leading to more accurate estimations of the mid-stance and heel loading stiffnesses. This could, also, enable modeling a portion of the spring beam elements with lower bending stiffness to account for the lower continuous fiber content caused by the spring-plantar junction. These improvements shall raise the possibility of obtaining the desired stiffness characteristics accurately. Moreover, stress analysis shall be performed for the design generated by the tool to confirm its strength. This is possible by remodeling the design using FE models that account for the explicit geometry of the sandwich structure, including the infill pattern. This will allow the estimation of the stresses in the skin and the core infill.

4 Conclusion

This study aimed to develop a numerical optimization tool to investigate potential designs for 3D-printed sandwich-structured composite foot prostheses as an alternative to laminated ones. The tool was based on beam finite elements to achieve an efficient optimization of various prosthesis shapes.

A commercially available laminated prosthesis was analyzed to predict its stiffness behavior under various loading conditions. This led to the definition of reference stiffness parameters for the designed 3D-printed prosthesis. Subsequently, the tool was used to solve a preliminary optimization problem for four distinct prosthesis types. These are C-shaped and J-shaped prostheses each of which with or without a heel-support. The preliminary optimization considered weight as the cost function.

It was found that the inclusion of a heel-support stiffens the prosthesis excessively, causing the solutions to suggest very thin structures, which are difficult to print. However, two feasible optimal solutions were obtained for the C-shaped and the J-shaped prosthesis without a heel-support.

The tool was then used to refine the design of the C-shaped prosthesis without a heel-support by solving a design problem with multiple design constraints. It was possible to obtain a design matching three of the reference stiffness parameters.

However, the obtained design demonstrated different stiffness behavior, when analyzed using plane stress finite elements. This was mainly due to the simplification considered in modeling the geometry of the junction between the integrated components (spring-plantar junction) of the prosthesis in the beam finite elements. Another reason was that the C-shape induces compressive stresses in the core of the sandwich structure, which are not accounted for in beam finite element modeling. These represent the limitations of the current optimization tool, which could be overcome in future works, considering more detailed modeling approaches. Therefore, the current tool only serves as a rapid and versatile approach for making preliminary design decisions in the emerging field of developing 3D-printed composite foot prostheses.

5 Acknowledgements

The authors are grateful to Centro Protesi INAIL for supporting this study through the PROFIL Project (FILamenti multimateriali per la realizzazione di PROtesi personalizzate ad alte prestazioni con focus su adaptive sport).

6 References

[1] Kumar PK, Charan M, Kanagaraj S. Trends and Challenges in Lower Limb Prosthesis. IEEE Potentials 2017;36:19–23. https://doi.org/10.1109/MPOT.2016.2614756.
[2] Coalition-Amputee. Prosthetic Feet Fact Sheet 2016:1–3. https://www.amputee-coalition.org/resources/prosthetic-feet/ (accessed August 27, 2023).
[3] Wezenberg D, Cutti AG, Bruno A, Houdijk H. Differentiation between solid-ankle cushioned heel and energy storage and return prosthetic foot based on step-to-step transition cost. J Rehabil Res Dev 2014;51:1579–90. https://doi.org/10.1682/JRRD.2014.03.0081.
[4] Scholz MS, Blanchfield JP, Bloom LD, Coburn BH, Elkington M, Fuller JD, et al. The use of composite materials in modern orthopaedic medicine and prosthetic devices: A review. Compos Sci Technol 2011;71:1791–803. https://doi.org/10.1016/j.compscitech.2011.08.017.
[5] Randbaran E, Dayang L, Zahari R, Sultan M, Mazlan N. Advantages and Disadvantages of Using Composite Laminates in The Industries. Mod Approaches Mater Sci 2020;3:349–52. https://doi.org/10.32474/mams.2020.03.000158.
[6] Brent Strong A. Fundamentals of composites manufacturing - materials, methods and applications. 2nd ed. Dearborn, Mich. : Society of Manufacturing Engineers; 2008.
[7] Chen RK, Jin Y an, Wensman J, Shih A. Additive manufacturing of custom orthoses and prostheses-A review. Addit Manuf 2016;12:77–89. https://doi.org/10.1016/j.addma.2016.04.002.
[8] Kostovic M, Rollo G, Sorrentino A, Ticli E, De Capitani C, Pittaccio S, et al. A Multidisciplinary Approach for the Designing and Realization of Customized High Performance Prostheses by Continuous Fiber Additive Manufacturing. In: Miesenberger K, Kouroupetroglou G, Mavrou K, Manduchi R, Rodriguez M, Penáz P, editors. 18th Int. Conf. ICCHP-AAATE, vol. 13342 LNCS, Lecco: Springer International Publishing; 2022, p. 379–86. https://doi.org/10.1007/978-3-031-

08645-8_44.
[9] Parandoush P, Lin D. A review on additive manufacturing of polymer-fiber composites. Compos Struct 2017;182:36–53. https://doi.org/10.1016/j.compstruct.2017.08.088.
[10] Faustini MC, Crawford RH, Neptune RR, Rogers WE, Bosker G. Design and analysis of orthogonally compliant features for local contact pressure relief in transtibial prostheses. J Biomech Eng 2005;127:946–51. https://doi.org/10.1115/1.2049331.
[11] South BJ, Fey NP, Bosker G, Neptune RR. Manufacture of energy storage and return prosthetic feet using selective laser sintering. J Biomech Eng 2010;132:1–6. https://doi.org/10.1115/1.4000166.
[12] Yap J, Renda G. Low-cost 3D-printable prosthetic foot. Third Eur. Conf. Des., 2015.
[13] Ahmed MH, Jamshid A, Amjad U, Azhar A, Hassan MZ ul, Tiwana MI, et al. 3D Printable Thermoplastic Polyurethane Energy Efficient Passive Foot. 3D Print Addit Manuf 2022:1–10. https://doi.org/10.1089/3dp.2021.0022.
[14] Fanaroff AC, Yang L, Nathan AS, Khatana SAM, Julien H, Wang TY, et al. Geographic and socioeconomic disparities in major lower extremity amputation rates in metropolitan areas. J Am Heart Assoc 2021;10. https://doi.org/10.1161/JAHA.121.021456.
[15] Isobe T, Tanaka T, Nomura T, Yuasa R. Comparison of strength of 3D printing objects using short fiber and continuous long fiber. IOP Conf Ser Mater Sci Eng 2018;406. https://doi.org/10.1088/1757-899X/406/1/012042.
[16] Bandyopadhyay A, Heer B. Additive manufacturing of multi-material structures. Mater Sci Eng R Reports 2018;129:1–16. https://doi.org/10.1016/j.mser.2018.04.001.
[17] Shahar FS, Hameed Sultan MT, Lee SH, Jawaid M, Md Shah AU, Safri SNA, et al. A review on the orthotics and prosthetics and the potential of kenaf composites as alternative materials for ankle-foot orthosis. J Mech Behav Biomed Mater 2019;99:169–85. https://doi.org/10.1016/j.jmbbm.2019.07.020.
[18] Kamel H, Harraz O, Azab K, Attia T. Developing an Optimized Low-Cost Transtibial Energy Storage and Release Prosthetic Foot Using Three-Dimensional Printing. J Eng Sci Med Diagnostics Ther 2020;3:1–9. https://doi.org/10.1115/1.4046319.
[19] Li C, Pisignano D, Zhao Y, Xue J. Advances in Medical Applications of Additive Manufacturing. Engineering 2020;6:1222–31. https://doi.org/10.1016/j.eng.2020.02.018.
[20] Fey NP, South BJ, Seepersad CC, Neptune RR. Topology optimization and freeform fabrication framework for developing prosthetic feet. 20th Annu Int Solid Free Fabr Symp SFF 2009 2009:607–19.
[21] Rochlitz B, Pammer D. Design and analysis of 3D printable foot prosthesis. Period Polytech Mech Eng 2017;61:282–7. https://doi.org/10.3311/PPme.11085.
[22] Porras F, Araya M, Sánchez O, Vargas R, Corrales S, Aplicada LDE, et al. Structural static characterization of a novel 3D printed prosthetic foot. Addit Manuf Meets Med 2020;2:3–4. https://doi.org/10.18416/AMMM.2020.2009009.
[23] ISO. BSI Standards Publication Prosthetics — Testing of ankle- foot devices and foot units — Requirements and test methods (ISO 22675 : 2016). vol. 22675:2016. 2016.
[24] Halsne EG, Czerniecki JM, Shofer JB, Morgenroth DC. The effect of prosthetic foot stiffness on foot-ankle biomechanics and relative foot stiffness perception in people with transtibial amputation. Clin Biomech 2020;80. https://doi.org/10.1016/j.clinbiomech.2020.105141.
[25] Fey NP, Klute GK, Neptune RR. The influence of energy storage and return foot stiffness on walking mechanics and muscle activity in below-knee amputees. Clin Biomech 2011;26:1025–32. https://doi.org/10.1016/j.clinbiomech.2011.06.007.
[26] Kathrotiya D, Yusuf A, Bhagchandani RK, Gupta S. A Study for the development of prosthetic foot by additive manufacturing. J Brazilian Soc Mech Sci Eng 2023;45. https://doi.org/10.1007/s40430-023-04107-y.
[27] Warder HH, Fairley JK, Coutts J, Glisson RR, Gall K. Examining the viability of carbon fiber reinforced three-dimensionally printed prosthetic feet created by composite filament fabrication. Prosthet Orthot Int 2018;42:644–51. https://doi.org/10.1177/0309364618785726.
[28] American Orthotic & Prosthetic Association. AOPA'S PROSTHETIC FOOT PROJECT. 2010.
[29] Olesnavage KM, Prost V, Johnson WB, Amos Winter VG. Passive prosthetic foot shape and size optimization using lower leg trajectory error. J Mech Des Trans ASME 2018;140. https://doi.org/10.1115/1.4040779.
[30] Olesnavage KM, Winter AG. A Novel Framework for Quantitatively Connecting the Mechanical Design of Passive Prosthetic Feet to Lower Leg Trajectory. IEEE Trans Neural Syst Rehabil Eng

2018;26:1544–55. https://doi.org/10.1109/TNSRE.2018.2848845.
[31] Galati M, Viccica M, Minetola P. A finite element approach for the prediction of the mechanical behaviour of layered composites produced by Continuous Filament Fabrication (CFF). Polym Test 2021;98. https://doi.org/10.1016/j.polymertesting.2021.107181.
[32] Kabir SMF, Mathur K, Seyam AFM. A critical review on 3D printed continuous fiber-reinforced composites: History, mechanism, materials and properties. Compos Struct 2020;232. https://doi.org/10.1016/j.compstruct.2019.111476.
[33] Olesnavage KM, Prost V, Johnson WB, Major MJ, Winter AG. Experimental Demonstration of the Lower Leg Trajectory Error Framework Using Physiological Data as Inputs. J Biomech Eng 2021;143. https://doi.org/10.1115/1.4048643.
[34] Arteiro A, Furtado C, Catalanotti G, Linde P, Camanho PP. Thin-ply polymer composite materials: A review. Compos Part A Appl Sci Manuf 2020;132. https://doi.org/10.1016/j.compositesa.2020.105777.
[35] Turon A, Camanho PP, Costa J, Dávila CG. A damage model for the simulation of delamination in advanced composites under variable-mode loading. Mech Mater 2006;38:1072–89. https://doi.org/10.1016/j.mechmat.2005.10.003.
[36] Ma Y, Li Y, Liu L. Off-Axis Tension Behaviour of Unidirectional PEEK/AS4 Thermoplastic Composites. Appl Sci 2023;13. https://doi.org/10.3390/app13063476.
[37] MATLAB. R2020a 2020.
[38] Dassault Systèmes. Abaqus 2021 manual n.d.
[39] Timoshenko S, Young D. Elements of strength of materials. 5th ed. D. Van Nostrand; 1968.
[40] Chou P, Carleone J, Hsu C. Elastic Constants of Layered Media. J Compos Mater 1972;6:80–93.
[41] Shepherd MK, Gunz D, Lecomte C, Rouse EJ. Methods for describing and characterizing the mechanical behavior of running-specific prosthetic feet. IEEE Int Conf Rehabil Robot 2019;2019-June:892–8. https://doi.org/10.1109/ICORR.2019.8779557.
[42] Adamczyk PG, Roland M, Hahn ME. Sensitivity of biomechanical outcomes to independent variations of hindfoot and forefoot stiffness in foot prostheses. Hum Mov Sci 2017;54:154–71. https://doi.org/10.1016/j.humov.2017.04.005.
[43] Össur. Pro-Flex® XC n.d. https://www.ossur.com/en-us/prosthetics/feet/pro-flex-xc (accessed January 15, 2022).
[44] Össur. Vari-Flex® n.d. https://www.ossur.com/en-us/prosthetics/feet/vari-flex (accessed June 9, 2023).
[45] Markforged. Composites Data Sheet 2021:0–1.
[46] Martulli LM, Sala R, Rollo G, Kostovic M, Lavorgna M, Sorrentino A, et al. Preliminary Stiffness-Driven Redesign of a Laminated Prosthetic Component Using Additive Manufacturing. Polymers (Basel) 2023;15:1–15. https://doi.org/10.3390/polym15020346.
[47] Markforged. Design Guide for 3D Printing with Composites. 2020.
[48] Peng C, Fox K, Qian M, Nguyen-Xuan H, Tran P. 3D printed sandwich beams with bioinspired cores: Mechanical performance and modelling. Thin-Walled Struct 2021;161. https://doi.org/10.1016/j.tws.2021.107471.
[49] Minus ML, Kumar S. The processing, properties, and structure of carbon fibers. Jom 2005;57:52–8. https://doi.org/10.1007/s11837-005-0217-8.
[50] Markforged Eiger software n.d. https://markforged.com/software (accessed February 1, 2022).
[51] Shepherd MK, Gunz D, Clites T, Lecomte C, Rouse EJ. Designing Custom Mechanics in Running-Specific Prosthetic Feet via Shape Optimization. IEEE Trans Biomed Eng 2023;70:747–55. https://doi.org/10.1109/TBME.2022.3202153.